

# Investigation on effect of colloidal nano-silica on the strength and durability characteristics of red mud blended Portland cement paste through tortuosity

✉K. Athira, ✉T. Shanmugapriya✉

School of Civil Engineering, VIT, Vellore, (Tamil Nadu, India)  
✉: shanmugapriya.t@vit.ac.in

Received 28 February 2022

Accepted 23 May 2022

Available on line 5 September 2022

**ABSTRACT:** A novel binder system for cement-based composites depending upon the strength and durability characteristics is introduced in this study. The possibility of calcined red mud cement pastes with and without colloidal nano-silica (CNS) over Ordinary Portland Cement paste (OPC) at three W/B ratios (0.3, 0.4, 0.5) is evaluated. The optimum percentage of cement replacement by red mud (15%) was selected from compressive strength values of different cement replacements (5%, 10%, 15%, and 20%). Colloidal nano-silica (CNS) was added at 0.5%, 1%, 1.5%, and 2 % to the selected red mud cement paste. Water absorption, sorptivity, resistance to sulfate attack, and resistance to acid attack tests were conducted for optimum red mud cement paste with and without CNS. The experimental results are explained based on tortuosity with empirical formulas and mathematical models of pore network distribution. The tortuosity is directly proportional to the inter-connectivity of the pores. The mixes with 15% calcined red mud and 1.5% CNS replacement performed better strength and durability at all W/B ratios. The mix (R15NS1.5) with minimum tortuosity value results in the higher overall performance of the paste. The mixes with a 0.3 W/B ratio give high-performance cement paste compared to higher W/B ratios.

**KEY WORDS:** Porosity; Pore structure distribution; Tortuosity; Mechanical strength; Durability.

**Citation/Citar como:** Athira, K.; Shanmugapriya, T. (2022) Investigation on effect of colloidal nano-silica on the strength and durability characteristics of red mud blended Portland cement paste through tortuosity. Mater. Construcc. 72 [347], e293. <https://doi.org/10.3989/mc.2022.01922>.

**RESUMEN:** *Investigación sobre el efecto de la nanosilice coloidal en las características de resistencia y durabilidad de la pasta de cemento Portland mezclada con lodo rojo mediante estudios de tortuosidad.* En este estudio se presenta un nuevo sistema aglomerante para compuestos en base cemento que depende de las características de resistencia y durabilidad. Se evalúa la posibilidad de incluir pastas de cemento de lodo rojo calcinado con y sin nanosilice coloidal (CNS) en pastas de cemento Portland ordinario (OPC) en tres relaciones a/b (0,3, 0,4, 0,5). El porcentaje óptimo de reemplazo de cemento por lodo rojo (15 %) se seleccionó de los valores de resistencia a la compresión obtenidos entre los diferentes reemplazos de cemento considerados (5 %, 10 %, 15 % y 20 %). Se añadió nanosilice coloidal (CNS) al 0,5 %, 1 %, 1,5 % y 2 % a la pasta de cemento de lodo rojo seleccionada. Se realizaron pruebas de absorción de agua, sorción, resistencia al ataque de sulfatos y resistencia al ataque de ácidos para obtener una pasta de cemento de lodo rojo óptima con y sin CNS. Los resultados experimentales se explican basados en parámetros de tortuosidad con fórmulas empíricas y modelos matemáticos de distribución de redes de poros. La tortuosidad es directamente proporcional a la interconectividad de los poros. Las mezclas con 15% de lodo rojo calcinado y 1,5% de reemplazo de CNS presentaron mejor resistencia y durabilidad en todas las relaciones a/b. En la mezcla (R15NS1.5) con un valor mínimo de tortuosidad se obtiene el mayor rendimiento general de la pasta. Las mezclas con una relación a/b de 0,3 generan una pasta de cemento de alto rendimiento en comparación con relaciones a/b más altas.

**PALABRAS CLAVE:** Porosidad; Distribución de la estructura porosa; Tortuosidad; Resistencias mecánicas; Durabilidad.

**Copyright:** ©2022 CSIC. This is an open-access article distributed under the terms of the Creative Commons Attribution 4.0 International (CC BY 4.0) License.

## 1. INTRODUCTION

Red mud is a waste produced in the aluminum manufacturing industry. One tonne of aluminum produces approximately 2-3 tonnes of red mud (1). The constituent presented in red mud depends upon the compounds in the raw material (bauxite), parent mineral, and compounds introduced during the manufacturing process. The main threats in the handling of this industrial waste are the high pH (>11), alkaline airborne dust emissions, safety storage problems, alkali seepage into underground water, and the large area of land required for disposal (1).

The effective disposal of red mud is done by disposing it into seawater after neutralization and dry and wet stack piling on land. A large amount of alkaline solution, and the leaching of toxic and radioactive elements from the deposit, can lead to the disintegration of the balance of the aquatic environment (2). Therefore, landfilling is the widely used mode of discarding this industrial waste. The spillage of the red mud storage reservoir in Ajka (Hungary) on October 4, 2010, has raised concerns over the disposal of the red mud by landfilling technique. High monitoring and maintenance are needed to eliminate the probability of such catastrophic failures. High cost, land requirement, and non-availability of environmental experts are the major threats to landfilling methods. India alone spends around 150 million USD to dispose of an output of 10 million tons of red mud per year (2). Apart from landfilling, recycling and recovery are the two other methods for disposal. In the recycling industry, red mud is used in the construction field as a cement replacement and as a raw material in manufacturing bricks and pavement tiles. In many developing countries, the limited availability of economic resources inspired an exploration of the adsorption properties of heavy metal ions from wastewater. It provided a double benefit to the environment by the metal recovering property of raw/modified red mud. However, only 10% of the red mud produced is used for recycling and recovery due to the unavailability of standards, high transportation costs, and cheaper alternate sources. Almost all the countries adopt more or less all the above three methods simultaneously (1, 2).

India is the 3<sup>rd</sup> largest producer of primary aluminum and the 7<sup>th</sup> largest bauxite reserve globally. According to the Ministry of Mines, in India, growth in aluminum production is 3.3 MMT in 2017-18, 5.3 MMT in 2020-21, and is expected to grow by 7.2 MMT in the next five years (2). The by-products of the manufacturing process constitute more solid waste than aluminum during its making. To implement the zero-waste concept, the waste should be converted into augmented products (2). Therefore, National Institution for Transforming India (NITI) Aayog has recommended considering the significance of red mud as a secure and favorable secondary raw material. Thus, there is a contingency to consider the technical, environmental,

and economic feasibility of employing red mud as a value-added product.

The chemical composition of red mud is similar to cement (3-5). Therefore, it is used as a binder material in different studies and is used in concrete by replacing cement (4). The composition of red mud may not vary according to the source of bauxite (3). Red mud is used to produce fine aggregate (6-8), coarse aggregate (9), Calcium Sulfo Aluminate (CSA) cement in combination with silica fume (10), pavements, subgrade materials, production of cement clinker, and geopolymer concrete (11, 12). An optimum of 2.5% to 5% cement replacement by red mud in cement composites was found with good mechanical and durability properties in lightweight concrete and self-compacting concrete, respectively (5, 13). A 25% filler replacement with red mud gave better durability properties such as better electrical (14) and chloride penetration resistance (15). Recently, diagnostic X-Ray shielding tiles were developed with processed red mud, which is capable of replacing lead-based radiation shielding products (16).

The chemical compound proportion of red mud is sound enough to produce an excellent cementitious product. However, high porosity and water demand limit the utilization of red mud concrete as structural elements. Therefore, the current applications of red mud concrete are limited to the construction of pavements and subgrade materials (11, 12). Therefore, investigating pore structure distribution is highly essential to establish the red mud as a construction material. Using MIP (Mercury Intrusion Porosimetry) for measuring porosity involves expensive and complex procedures (17). Consequently, tortuosity is an indirect parameter to define the pore structure distribution (18). The strength and durability properties based on tortuosity are explained mathematically with the support of experimental results in this investigation.

Nowadays, nano-silica is introduced in cement composites for better strength and durability (19). The influence on fresh and hardened properties of cement composites by the addition of nano-silica powder and colloidal nano-silica (CNS) was studied (20-22). Nano-silica powder gets agglomerates in the cement matrix creating weaker areas, and the previous studies support the use of CNS for better performance as cement replacement material (21). Generally, nano-silica acts as nucleation of hydration and results in the extension of silica sheets in the C-S-H gel and enhances the strength of the specimens (19). Nanoparticles refine the pore structure, reduce the calcium leaching, maintain the Ca/Si ratio in the pore solution (23), and thereby improve the durability of the cement composites such as resistance to acid attack (19), sulfate attack, and chloride penetration (24). Kong *et al.* (2015) explained the possibility of cement replacement with colloidal nano-silica (CNS) to enhance the hydration process by reducing the total porosity (21).

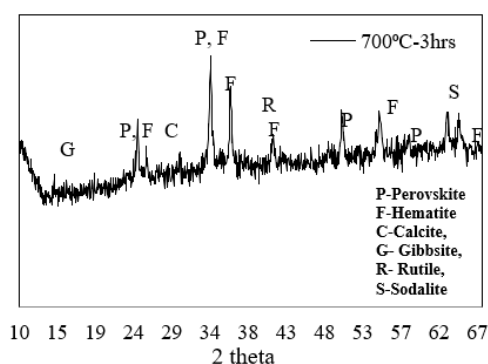
In this investigation, the introduction of CNS to red mud cement pastes and the effect on the mechanical and durability properties are considered. Strength and durability studies were conducted for red mud blended OPC with and without the addition of CNS. The cement paste is developed by analyzing the porosity and tortuosity of the paste matrix. Pore radius from the capillary action was estimated, and the fluid ingress concerning tortuosity in red mud cement paste with CNS was examined. The results were analyzed and explained with the mathematical models.

### 1.1. Materials

In this study, OPC 53 grade cement with a surface area of 330 m<sup>2</sup>/kg and a mean particle size of about 10µm was used. Highly alkaline bauxite residue (red mud) from HINDALCO Belgaum was used to prepare laboratory-scale binding material rich in hematite and alumina. The amount of and present in the raw sample is significantly less. Therefore, to improve the percentage, the red mud was calcined at 700°C. The chemical composition of raw red mud and calcined red mud is given in Table 1.

TABLE 1. Chemical composition in raw red mud and calcined red mud.

Compounds	% by mass (Raw red mud)	% by mass (Red mud calcined at 700°C)
Al <sub>2</sub> O <sub>3</sub>	17.8	30.4
Fe <sub>2</sub> O <sub>3</sub>	45	22.0
SiO <sub>2</sub>	8	21.8
TiO <sub>2</sub>	10	3.28
Na <sub>2</sub> O	4	11.6
CaO	2	5.6



The powder XRD and FTIR of calcined red mud are shown in Figure 1. Sharp peaks of X-ray diffraction patterns (XRD) are mainly due to the presence of perovskite (CaTiO<sub>3</sub>), hematite (Fe<sub>2</sub>O<sub>3</sub>), gibbsite (Al(OH)<sub>3</sub>), calcite (CaCO<sub>3</sub>), rutile (TiO<sub>2</sub>), and sodalite (Na<sub>2</sub>O·Al<sub>2</sub>O<sub>3</sub>·SiO<sub>2</sub>). Calcination decomposes compounds and turns most crystalline structures to the amorphous phase (11) which readily reacts with water and Portland cement to form C-S-H gel.

The FTIR spectra of phase transformation of red mud calcined at 700°C are defined in Figure 1b. Peaks at ~1510–1410 cm<sup>-1</sup> and ~873–1630 cm<sup>-1</sup>, represent O-C-O's symmetric stretching vibration. The absorption band at ~650–550 cm<sup>-1</sup> gave Al-O-Si asymmetric stretching vibration and symmetric vibration of Si-O-Si. At ~470–460 cm<sup>-1</sup>, bending vibrations of Si-O-Si and O-Si-O are obtained.

Colloidal nano-silica (Levasil CB8) contains 50% by weight solids and has a specific gravity of 1.03. The average particle size and specific surface area of nano-silica are 20nm and 86 m<sup>2</sup>/g. The specimens underwent some characteristic studies to analyze the crystallinity of the structure, pore structure, and hydration products. A polycarboxylic ether (PCE) based superplasticizer (SP) was used to acquire a target spread of 14 to 15cm in the mini-slump cone test at a 0.3 W/B ratio.

### 1.2. Mix proportions

Table 2 presents nine mix proportions of red mud-cement paste mixes with and without CNS at three W/B ratios. The red mud in this study was optimized to ensure better compressive strength from a set of trial mixes with different cement replacements (0% to 20%). CNS was added at 0.5% to 2% with 0.5% interval by weight of optimum red mud cement mixes. CNS was stirred with water for 3 min to obtain homogenous dispersion of the nanoparticles.

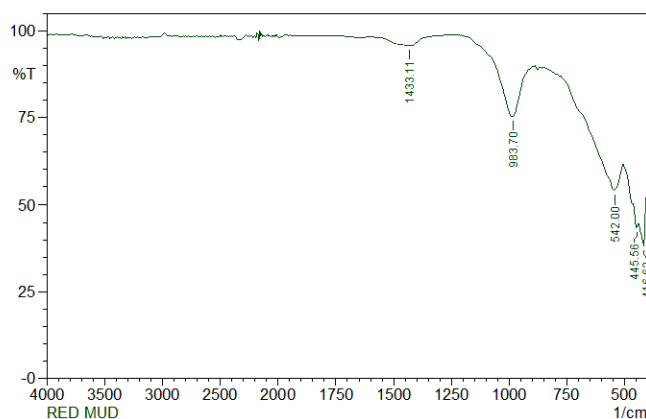


FIGURE 1. (a) XRD and (b) FTIR spectra of calcined red mud.

TABLE 2. Mix proportion.

Mix designation	Cement	Red mud	Nano-sil-ica	SP dosage for W/B-0.3(% by weight of binder)
R0NS0	100	-	-	0.125
R5NS0	95	5	-	0.375
R10NS0	90	10	-	0.375
R15NS0	85	15	-	0.625
R20NS0	80	20	-	0.875
R15NS0.5	84.5	15	0.5	0.500
R15NS1	84	15	1	0.375
R15NS1.5	83.5	15	1.5	0.375
R15NS2	83	15	2	0.250

Superplasticizer dosage was adjusted to maintain the constant fluidity of all mixes. The optimum superplasticizer dosage was adopted to conserve the constant flowability of the mixes for a W/B ratio of 0.3. However, mixes with 0.4 and 0.5 W/B ratios achieved satisfactory workability with the proposed water content. The constituents were added to the mortar mixer and mixed for 4-5 minutes. The homogenous mix was poured into the molds of standard dimensions and retained for 24 h. Normal water curing was carried out for the specimens to reach the various period of testing.

### 1.3. Experimental methods

The compressive strength test of cubes cured for 28-day was conducted as per IS 516-2018 (25). Cement paste cubes of 50 mm size were prepared for the investigation. The testing was done in a compression testing machine with 3000 kN (accuracy of  $\pm 1\%$ ).

The effect of water absorption, bulk density, and permeable pore space of red mud-cement pastes on the addition of CNS was studied as per ASTM C-642-13 (26). The red mud-cement paste specimens were tested for capillary water absorption as per ASTM C1585-13. The cement paste specimens were placed in a tray filled with normal water. The water was allowed to enter through only one face of the specimen. The bottom of the specimen was immersed in water up to 2 mm in depth. The mass gain of specimens was measured (to an accuracy of 0.01 g) in the intervals mentioned in the code. By normalizing the value of the slope of the plot between capillary mass rise against the square root of time, the sorptivity index was calculated. Sorptivity was found from the slope of the curve obtained from the mass variation per area,  $I$  (mm), versus the square root of the time. The primary and secondary sorptivity were decided from the linear regression using successive points (27).

Standard sodium sulfate solution was prepared as per the ASTM C1012 (ASTM 2012b). The cubes of

dimensions ( $50 \times 50 \times 50$  mm) reached a curing age of 28-day, were weighed, and successively cured in a sodium sulfate solution. The effect of sulfate attack on the strength of red mud cement paste with and without CNS was analyzed by conducting the compressive strength test for 28, and 56-day sulfate cured specimens. The optical microscopic images did visual inspection of sulfate attack in the specimens. Specimens were cured in 0.5 mol/ L  $\text{HNO}_3$  with a  $\text{pH} \leq 3$  as per ASTM C1898. The specimens were tested for 28-day and 56-day acid curing.

## 2. RESULTS AND DISCUSSION

### 2.1. Compressive strength

Compressive strength was analyzed at 3, 7, and 28-days, red mud-cement pastes (W/B ratio of 0.30, 0.40, and 0.50). The compressive strength was decreased with the increase in red mud content. All the values obtained are less than the reference paste. The reduction of strength with the addition of red mud is mainly due to the increased porosity and the loose structure (5). The minimum reduction in compressive strength for 28-day curing concerning the reference mix was recorded in R15NS0 as 26%, 1%, and 11% at 0.3, 0.4, and 0.5 W/B ratios, respectively (Figure 2). Therefore, R15NS0 was the optimum mix for further studies with CNS addition.

The addition of CNS to R15NS0 from 0.5% to 1.5% enhances the strength gain of the red mud-cement paste for all W/B ratios. The change in compressive strength is not significant at the early curing ages (3 and 7 days). For instance, at a 0.3 W/B ratio, an increment in compressive strength from 0 to 1.2% concerning R0NS0 is observed in red mud cement mixes with CNS. However, with a cement paste of 28-day curing, an explicit increment of compressive strength was observed with the CNS addition compared to the red mud cement paste without

CNS (R15NS0). A maximum of 37%, 5%, and 35% strength increment at 0.3, 0.4, and 0.5 W/B ratios were recorded for R15NS1.5 than R15NS0 (Figure 2). The mixes with CNS achieve more or less the same compressive strength as the reference mix (R0NS0). CNS refined the pore network, and thereby the dense microstructure enhanced the compressive strength of the red mud cement paste (19). The addition of CNS of more than 1.5% to the red mud cement paste dropped the strength due to excessive fluid ingress from the colloidal suspension of nano-silica to the pore network of red mud cement paste structure to form gelatinous C-S-H (21). The result obtained from the current investigation agrees with the previous study conducted by Du and Pang (2019) (28). For further durability studies, there are six mixes (R0NS0, R0NS15, R15NS0.5, R15NS1, R15NS1.5, and R15NS2), including reference and optimum mixes are considered.

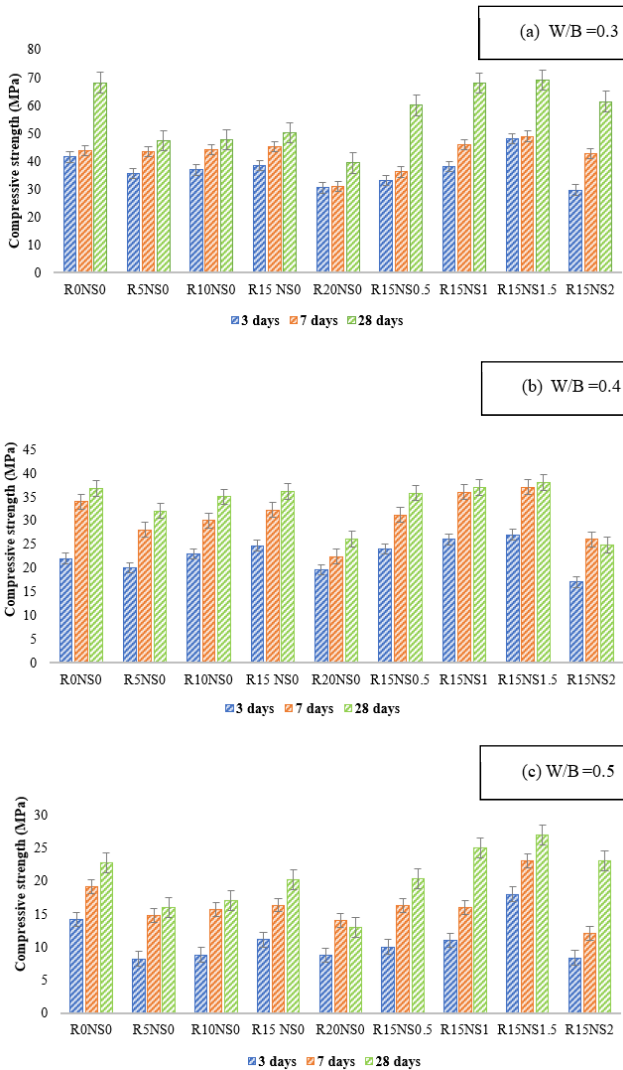


FIGURE 2. Compressive strength at 3, 7, and 28-days curing ages of mixes at a) 0.3 W/B ratio b) 0.4 W/B ratio c) 0.5 W/B ratio.

## 2.2. Water absorption and water permeable porosity

The water absorption test determined the water absorption, bulk density, and permeable pore space of 28-day cured red mud cement paste with and without CNS (Figure 3). The percentage of water absorption was continuously dropped from R15NS0.5 to R15NS1.5 for all W/B ratios. However, the results obtained are slightly higher than the R0NS0 and lower than the R15NS0. As the W/B ratio increased, the

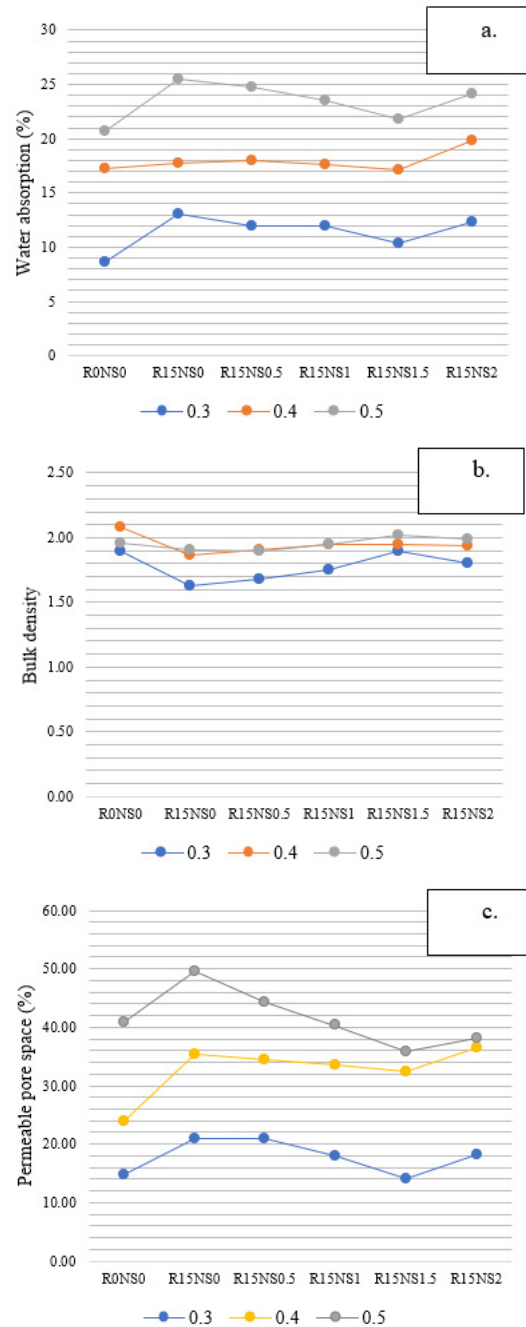


FIGURE 3. a) Water absorption. b) Bulk density. c) Permeable pore space (%) values of three W/B ratio.

percentage of water absorption also increased. Water got absorbed into the pore network and developed at higher W/B ratios. According to the previous study conducted by Kong *et al.* (2015), water absorption of cement composites should decrease when CNS is added to the mix. However, the red mud introduced to the cement matrix increased the permeable pore space of the mixture (Figure 3c). The percentage of water absorption was observed to be higher than the reference mix even after the addition of CNS. Minimum water absorption was found in R15NS1.5 and followed for all W/B ratios and gave 21%, 4%, and 15% lesser absorption to R15NS0 for 0.3, 0.4, and 0.5 W/B ratios (21). Compared to the other two mixes, the stable mixes were given by 0.4 W/B ratios. The maximum water absorption was reported by R15NS2 and is even greater than R15NS0. Figure 3b illustrates bulk density values of three water binder ratios. The bulk density followed the same trend as in water absorption and is increased with the increase in CNS addition. Maximum bulk density was observed in R15NS1.5 in all W/B ratios. The bulk density was reduced concerning the increment in the W/B ratio. Higher water-permeable pore volume connects the water absorption and bulk density. It reflects direct relation with water absorption and inverse to bulk density in each mix (Figure 3c). The lowest and highest percentage of permeable pore space was observed in R15NS1.5 and R15NS0, irrespective of the W/B ratios.

### 2.3. Sorptivity

The sorptivity results for the paste of 28-day curing are analyzed. The coefficient of sorptivity values for different W/B ratios are illustrated in Figure 4. Initial sorptivity measures water absorption through the interconnected capillary pores within the first six h. Secondary sorptivity is the water sorption through the pores in the next eight days. In this investigation, the observations are analyzed based on the primary sorptivity and secondary sorptivity graph slope.

The coefficient of initial sorptivity of R0NS0 shows a similar trend as in water absorption results. The primary and secondary sorptivity showed a lesser value than all other mixes. The addition of red mud increased the pore volume considerably. Therefore, the addition of CNS at a low percentage is insufficient to overcome the water ingress through the interconnected pore network. However, minimum primary (0.03, 0.68, 1.38) and secondary sorptivity (0.02, 0.13, 0.15) were found in R15NS1.5 for 0.3, 0.4, and 0.5 W/B ratios due to C-S-H gel formation and expansion to the capillary pores and the blockage of water transportation. The further addition of CNS to 2% slightly enhanced the sorptivity value to R15NS1.5 because of the fluid pressure developed in the pore solution and capillary pores by the excess fluid present in the CNS suspension.

At a 0.3 W/B ratio, minimum water-permeable pores and capillary pores existed because of the dense structure provided by hydration. Hence, the primary and secondary sorptivity have similar values for the consecutive mixes. Different sorptivity values were observed at 0.4 and 0.5 W/B ratios in each mix. Highly interconnected capillary pores were inferred for R15NS0 from the results. The trend obtained from the experimental observation contradicts the previous study, which explained the effect of CNS addition in the cement matrix. Du and Pang (2019) stated that the interconnectivity of the porous network was reduced due to the nanoparticle addition in the cement matrix (28). The improved pore distribution network due to the red mud addition shows enhanced sorptivity compared to the control mix. CNS particles occupy the extra pores created by red mud, which results in slightly high sorptivity to the control specimen. However, CNS adds a considerably low sorptivity to the red mud cement matrix. The entire primary and secondary water sorptivity results reduce as the W/B ratio decreases from 0.5 to 0.3 as the dense microstructure possessed by smaller W/B ratio mixes. Moreover, this decreases pores and a decrement in water ingress through the capillary pores.

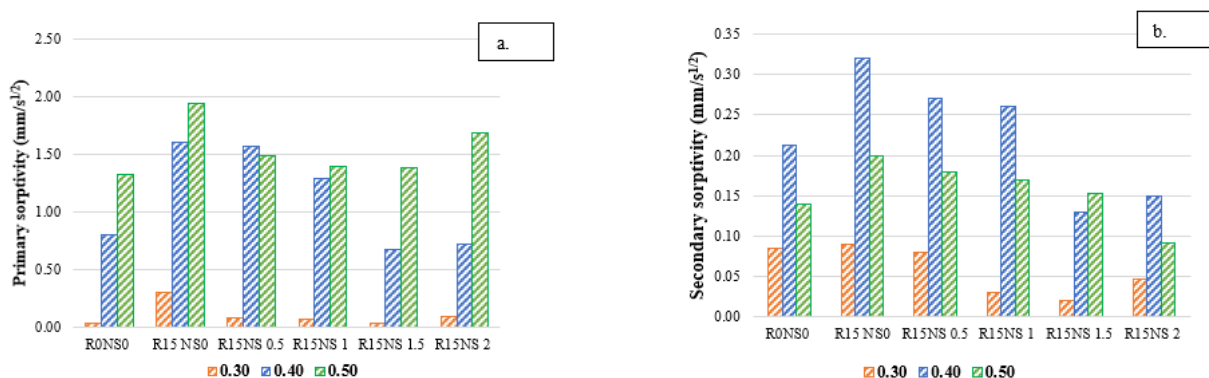


FIGURE 4. Coefficient of initial sorptivity ( $\text{mm/s}^{1/2}$ ) (a) and coefficient of secondary sorptivity ( $\text{mm/s}^{1/2}$ ) (b) of three W/B ratios 0.3, 0.4, 0.5.

### 2.4. Resistance to sulfate attack

Cement paste with 28-days of water curing was immersed in a 5% sodium sulfate solution prepared as per ASTM C1012 (ASTM 2012b). The specimens were tested for compressive strength after a specific immersion period of 28-day and 56-day in a sodium sulfate solution. Here, the variation in compressive strength was compared and analyzed with the 28-day compressive strength of the same mix. The change in compressive strength and weight behavior of specimens due to sulfate attack at three W/B ratios are in Figure 5.

It is noteworthy that at all W/B ratios, the control cement paste reported less resistance to sulfate attack. The compressive strength is highly affected due to the concentrated calcium hydroxide and sulfate ion reaction to produce gypsum, or the reaction between calcium aluminate hydrates and gypsum to form ettringite (29). The formation and deposition of ettringite, gypsum (chemical erosion products), and thenardite (physical erosion product) in the reference mix exhibit a gain in weight for all W/B ratios (30). In the calcined red mud (700°C), the amorphous calcium hydroxide is not available for the reaction with sulfate (Figure 1a). The addition of CNS further decreases

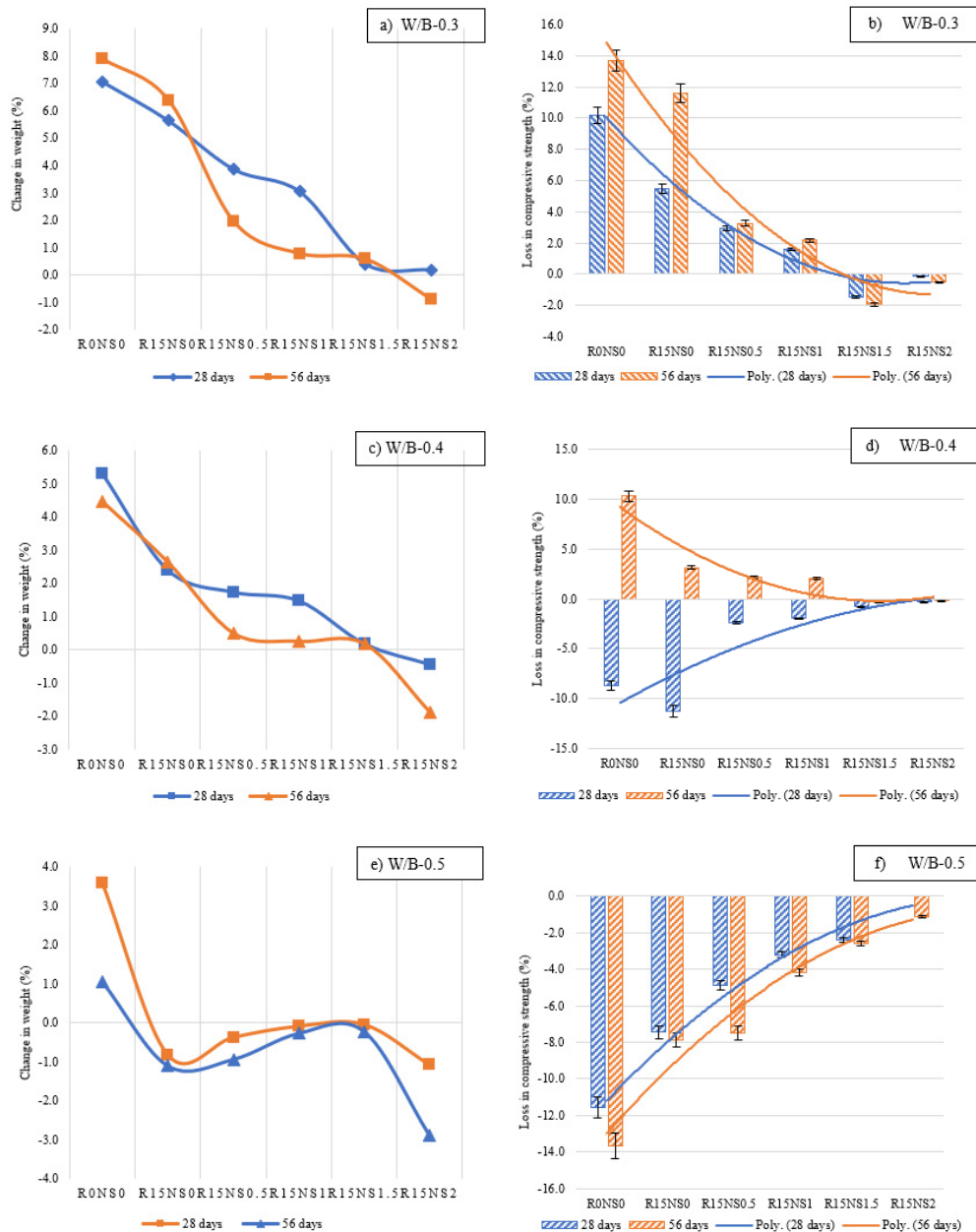


FIGURE 5. The loss in weight (%) for a) 0.3 W/B ratio, c) 0.4 W/B ratio, e) 0.5 W/B ratio; The loss in compressive strength (%) for b) 0.3 W/B ratio, d) 0.4 W/B ratio, f) 0.5 W/B ratio.

the availability of calcium hydroxide to react with sodium sulfate (31).

The red mud cement paste mixes with and without CNS showed relatively lesser weight gain due to salt deposition and loss in compressive strength at all W/B ratios. At a 0.3 W/B ratio, the maximum and minimum percentage of weight change (7.9% and -0.9%) and loss in compressive strength (13.7% and -0.1%) were recorded in R0NS0 and R15NS2, respectively (Figure 5a and Figure 5b). The compressive strength of the specimens starts decreasing very slowly or remains constant after sulfate curing due to the resistance of dense microstructure to sulfate attack (32). However, the compressive strength increased first and then decreased at 0.4 W/B ratios and continuously increased at 0.5 W/B ratios (Figure 5d, Figure 5f). At higher W/B ratios, the specimens contain more void spaces, and the hydration process continues when the curing proceeds. The phenomena are explained based on the prolonged C-S-H gel formation extended to the vacant pore space in red mud cement paste at 0.4 and 0.5 W/B ratios. The loss in compressive strength and change in weight is negligibly small in R15NS2 for entire W/B ratios (29). The addition of red mud and CNS into the cement paste enhanced the resistance to sulfate attack and attained stability in the aggressive chemical environment.

The addition of red mud decreased the loss in compressive strength due to the reduced calcium hydroxide content. The CNS particles occupied the capillary pores and blocked the fluid ingress through the pore network. Therefore, the weight gain and loss in compressive strength decreased significantly, and the specimen attained stability in the sulfate solution. The highest resistance to sulfate attack is observed in R15NS2 at 0.3 W/B ratios.

## 2.5. Resistance to acid attack

Specimens were cured in 0.5mol/L solution with a  $\text{pH} \leq 3$ . Highly soluble calcium nitrate ( $\text{Ca}(\text{NO}_3)_2$ ) salts were formed at the surface of the hardened cement paste. The low pH of the surrounding acid solution changed to 10.6, which is equivalent to the highly alkaline unaffected red mud cement paste. The weight

loss due to acid attack is given in Figure 7. Reference cement paste exhibits an enhanced calcium leaching in the acidic environment due to diffusion of the ion to the pore solution and the reduction of the pH of the pore solution. CNS occupied in the permeable pore structure of the red mud cement paste matrix decreases the calcium leaching and thereby maintained the Ca/Si ratio in the pore solution. A solid and extended silicate chain in C-S-H gel also helps in stabilizing the Ca/Si ratio in the pore solution in an aggressive acidic environment (19).

A maximum percentage loss in weight was observed in R0NS0 as 0.8%, 2.13%, and 3.46% at 0.3, 0.4, and 0.5 W/B ratios respectively. At all W/B ratios, the addition of CNS decreased the loss in the density of the specimens, and R15NS1.5 exhibited high stability and resistance to the acid attack. The minimum loss in weight at 0.3, 0.4, and 0.5 W/B ratios was recorded in R15NS1.5 as 0%, 0.05%, and 0.09% (Figure 7).

White color patches (White ring) appeared due to the formation of heavy silica precipitates by CNS, which is visible in Figure 8e. At a 0.5 W/B ratio, due to high porosity and tortuosity, quick acid ingress was observed through the paste matrix (Figure 8b), and, thereby, the weight of the specimens decreased continuously (Figure 7c). Shallow surface cracks were developed, and the specimen became more porous due to the silica (Si), iron (Fe), and aluminum (Al) precipitates produced and the chemical shrinkage (Figure 8c). Similarly, due to the reaction of nitric acid with the hematite present in calcined red mud, brown ring patches were identified in the paste matrix and are given in Figure 8d (19). The cement replacement with red mud improved the stability of the specimen in the acid solutions. Nano-silica further decreased the leaching of the specimen and showed less weight loss. In acid solution, high stability was exhibited by R15NS1.5 with a less reduction in density than other mixes (Figure 7).

## 3. EMPIRICAL RELATIONS

The primary purpose of this study is to correlate the experimental results of red mud blended OPC with

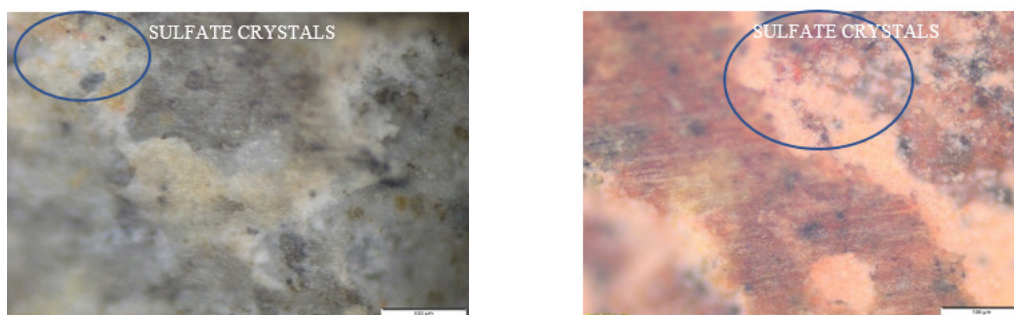


FIGURE 6. Optical microscopic images of sulfate attacked specimens.

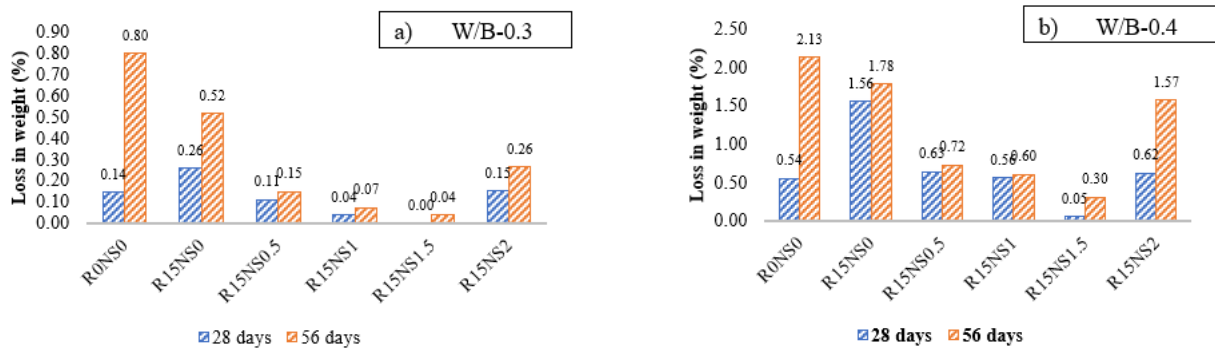


FIGURE 7. Weight loss percentage due to the acid attack of a) 0.3 b) 0.4 c) 0.5 W/B ratios.

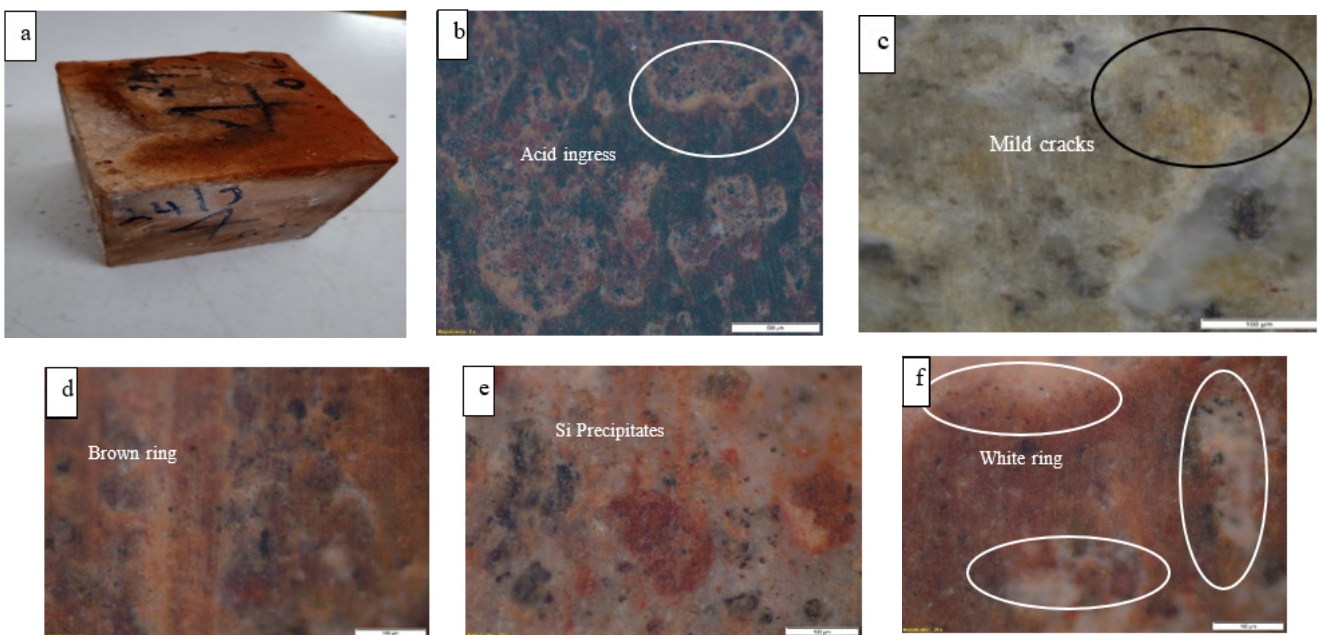


FIGURE 8. Optical microscopic images of acid ingress specimens.

the addition of CNS by the pore structure distribution and tortuosity ( $\tau$ ) with mathematical relations. The parameters are chosen from the previous studies and derived as per the requirement of the current investigation.

Here  
 Porosity ( $p$ ) =  $\frac{V_v}{V_s} * 100$

$V_v$  is the water permeable pore volume from the experimental results, and  $V_s$  is the total volume of the specimen.

### 3.1. Compressive strength vs Tortuosity

The relation of compressive strength with the porosity can be explained by the tortuosity ( $\tau$ ) of the pore network. The relation of  $\tau$  with the compressive strength of different mixes is illustrated

in Figure 9. The relationship between compressive strength and pore size distribution was explained by Kondraivendhan et al. (2013) in their study and is given in Equation [1] (18). The extent of tortuosity is extracted from the relationship between compressive strength and the pores size distribution given in Equation [1]. The  $\sigma$  is the compressive strength obtained from the experimental analysis,  $r$  is the mean pore radius, and  $p$  is the porosity.  $K$  value for each mix is calculated.

$$\sigma = K(c + rm) \frac{(1-p)}{\sqrt{r}} \quad [1]$$

$$\frac{\sigma \sqrt{r}}{(1-p)(c+m)} = \frac{pr^2 \rho g}{12 \mu \tau^2 (1 + \frac{1}{\alpha^2})} \quad [2]$$

Here  $\alpha$  is the aspect ratio of the pore. Considering Powers equation (32, 33):

$$p = \frac{\frac{w}{c} - 0.36\alpha}{\frac{w}{c} + 0.32} \quad [3]$$

$$\tau = \sqrt{\frac{(c+m)\rho g}{12\mu} \frac{p\alpha^2(1-p)r^{3/2}}{\sigma(\alpha^2+1)}} \quad [4]$$

Here  $\rho$  is the density, and  $\mu$  is the coefficient of viscosity of water. The relationship of compressive strength with  $\tau$  is given in Figure 9. Distinguishable pore diameter increments due to the extension of the W/B ratio from 0.3 to 0.5 give rise to a better  $\tau$ -value. To plot the graph of compressive strength versus  $\tau$ , the experimental results which satisfied in the sorptivity curve were considered. The value of  $\tau$  is inversely proportional to compressive strength. The tortuous nature of pores tends to occupy lengthy void space in the microstructure resulting in higher porosity than the theoretically calculated value and leading to the brittleness of the structure. Therefore, the study on the pore structure distribution based on tortuosity gives a better explanation for the reduced compressive strength of the addition of CNS in the red mud cement matrix. The relationship between compressive strength and tortuosity at a higher W/B ratio gives the value  $\tau$ . Increased compressive strength possesses lesser tortuosity.

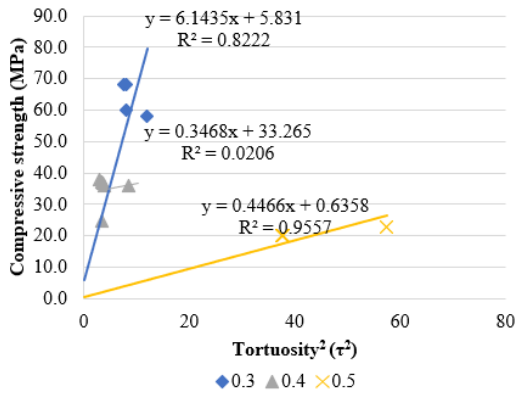


FIGURE 9. The relation of compressive strength with tortuosity.

### 3.2. Water absorption and water permeable porosity

Very close values of the percentage of water-permeable voids and the water absorption rate were obtained for the mixes with 0.3 W/B. The experimental result of water absorption does not follow any particular patterns with increased porosity. As the W/B ratio extends to 0.4 and 0.5, the relation between the parameters, as mentioned earlier, showed an apparent direct relationship with the addition of CNS. The best interaction of the water absorption with porosity (higher value for  $R^2$ ) was obtained for the mixes with

maximum W/B ratio. The porosity and water absorption hold a direct relationship (Figure 10). The rise in the W/B ratio increased the water-permeable pore volume and, hence, water absorption. The cement replacement with calcined red mud directly influences the porosity of the hardened paste and hence the rise of the water absorption rate. The higher specific surface area possessed by CNS also contributed to the escalation of water absorption of the mixes concerning the reference mix. However, in this research, only the influence of tortuosity is considered.

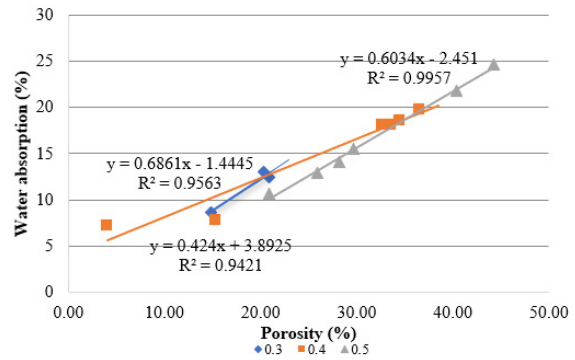


FIGURE 10. Relation between water absorption and porosity.

### 3.3. Sorptivity and pore radius

The tortuosity of the paste matrix and the inter-connectivity explain the variation in the sorptivity results. The porosity and pore radius calculated from the experimental data can express the coefficient of tortuosity for each mix. The calculated tortuosity value from the water-permeable porosity and pore radius can describe the variation in water ingressión better than the cumulative pore volume for porous materials like red mud.

Mixes with a high W/B ratio explicitly reduced water conductivity due to the capillary action. The pore radius has a spectacular influence on the water permeability. In a study conducted by Yang et al. (2019), the relationship between volumetric flow rate is defined in Equation [5] (35). According to Hagen-Poiseuille, assuming laminar flow through the capillary pores under a steady state, the volumetric flow rate is given in Equation [5]:

$$\frac{dQ}{dt} = \frac{\pi r^4 \Delta P}{8\mu h} \quad [5]$$

Here,  $\frac{dQ}{dt}$  is the volumetric flow rate,  $r$  = pore radius,  $\mu$  = viscosity of water,  $\Delta P$  = pressure drop, and  $h$  = distance penetration by the water or pore length.

Applying the capillary pressure in Equation [5]:

$$\frac{8\mu h}{r^2} \frac{dh}{dt} = \frac{2\sigma \cos\theta}{r} \quad [6]$$

The initial boundary conditions  $h=0, t=0$ :

$$\int dh = \int \frac{2\sigma \cos\theta}{8\mu} r dt$$

$$h = \sqrt{\frac{r\sigma \cos\theta}{2\mu}} \sqrt{t} \quad [7]$$

Here,  $\theta$  (wetting angle) is  $0^\circ$ , therefore  $\cos\theta = 1$  considering the mass, volume and density equation

$$\rho = \frac{m}{V}$$

$$m = A * h * p * \rho$$

Where  $A$  – surface area in contact with water,  $h$ = capillary rise (Equation [7]),  $p$ -water permeable porosity,  $\rho$ -density of water.

Substituting and rearranging:

$$r = \frac{1}{k} \left(\frac{S}{p}\right)^2 \quad [8]$$

$r$ -pore radius,  $S$ -initial sorptivity,  $p$ - water permeable porosity,  $k$ - proportionality constant.

Figure 10a illustrates a comparison between the porosity and the pore radius calculated from the experimental data. The results report that the porosity and pore radius does not hold a direct relation. The general assumption made in the Washburn equation about pore shape (cylindrical shape) is not always relevant for cement paste (Equation [6]) (36). Therefore, the porosity value does not explain the pore radius particularly, and the pore radius remains the same when the CNS is introduced regardless of porosity. Pore network distribution in terms of tortuosity is given in Figure 10b.

For further studies from the sorptivity graph has been taken into consideration. The sorption of the hardened paste structure depends upon the pore network distribution, which is explained based on the tortuosity of the pore structure. The given equation is extracted from the previous study to elucidate the

connection between pore diameter and tortuosity (33).

$$\ln \phi_{th} = -\tau \ln p + \ln \phi_0 \quad [9]$$

$\phi_{th}$  is the pore diameter at a particular porosity,  $\phi_0$  is the minimum pore diameter in the experiment,  $p$  is the porosity, and  $\tau$  is the tortuosity.

The tortuosity from the pore diameter was calculated from the experimental data (Equation [9]). The relationship between porosity and pore diameter is given in Figure 11a, and tortuosity is illustrated in Figure 11b. The pore diameter is exponentially related to the porosity calculated from the mathematical relations. When the pore diameter is minimum, the capillary action increases exponentially. The porosity calculated from the experimental results shows a direct relationship with the tortuosity. In this investigation, the porosity obtained is total porosity since the pore radius is not only the pore entry radius. The isolated pores are also assumed to be evaluated in this research by considering the total water-permeable pore volume by considering the weight. At all W/B ratios, the tortuosity is directly proportional to the porosity. The trend in strength and durability results can be correlated with the trend obtained in tortuosity.

### 3.4. Resistance to sulfate attack vs tortuosity

The tortuosity is extracted from Equation [8], assuming that the pore radius and the porosity values are the same. Figure 6 shows the sulfate crystals in the control mix and red mud developed in the tortuous pore structure. The crystal development hindered the interconnectivity of the pores, and the porosity changed accordingly. In Table 3, enhanced tortuosity values increase the possibility of entrapping the sulfate ion and reducing the specimen’s stability in the chemical environment, which can be related to the experimental data.

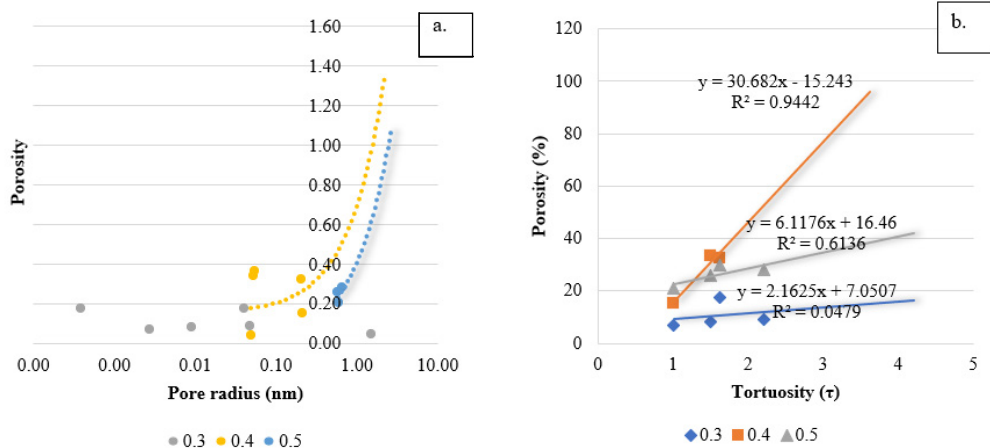


FIGURE 11. a) Influence of pore radius on porosity; b) connection between porosity and tortuosity.

TABLE 3. Tortuosity value from sulfate attack for different curing ages.

Mix designation	Tortuosity		
	28-day curing in water	28-day curing in 5% Na <sub>2</sub> SO <sub>4</sub> solution	56-day curing in 5% Na <sub>2</sub> SO <sub>4</sub> solution
<b>W/B-0.3</b>			
R0NS0	1.9	1.7	1.8
R15NS0	2.8	2.8	2.8
R15NS0.5	1.8	1.8	2.0
R15NS1	1.7	1.6	1.7
R15NS1.5	1.6	1.6	1.7
R15NS2	1.4	1.4	1.4
<b>W/B-0.4</b>			
R0NS0	2.7	2.9	3.9
R15NS0	3.6	3.7	3.7
R15NS0.5	3.3	3.1	3.4
R15NS1	2.8	2.0	2.5
R15NS1.5	2.1	1.5	1.9
R15NS2	2.6	1.4	1.8
<b>W/B-0.5</b>			
R0NS0	2.8	2.6	2.4
R15NS0	2.5	2.6	2.7
R15NS0.5	2.5	2.4	2.3
R15NS1	2.5	2.4	2.4
R15NS1.5	1.7	1.6	1.7
R15NS2	1.2	1.2	1.2

A higher value of tortuosity shows reduced stability of the specimens in the sulfate solution. The addition of red mud increased the  $\tau$  value concerning R0NS0. The addition of CNS reduced the  $\tau$  value, and the minimum was observed in R15NS2 for all W/B ratios. Here minimum  $\tau$  indicates the higher stability in sulfate solution, which can be related to the experimental results (33). The weight loss agrees with the  $\tau$  value and can be due to the high porous network and enhanced tortuosity created by spalling and the development of microcracks on the surface and the matrix.

#### 4. CONCLUSIONS

The following conclusions are drawn based on the experimental studies and results.

1) Cement replacement with calcined red mud at 700°C reduced the compressive strength of cement paste. An optimum of 15% cement replacement by red mud was obtained from compressive strength results considering the reference mix's minimum percentage reduction in strength.

2) The CNS addition to the optimum red mud cement paste enhanced the strength and durability properties. 1.5% addition of CNS with 15% red mud cement paste performed better in strength and durability.

3) Maximum and minimum percentage water absorption and volume of permeable pores were identified in R15NS0 and R15NS1.5, respectively. Primary and secondary sorptivity are directly proportional, and bulk density is inversely proportional to the water absorption and permeable pore volume at all W/B ratios.

4) The addition of red mud and CNS enhanced resistance to sulfate and acid attack of cement paste. R15NS2 showed the highest resistance to sulfate attack by exhibiting minimum weight change due to salt deposition and loss in compressive strength. Whereas R15NS1.5 showed better resistance to acid attack with minimum spalling and cracking. The visual examination with light optical microscopic images of eroded specimens defined the deformations in strength and density. High deposits of salt, mid cracks, and formations of chemical reactions were identified, indicating the paste's instability in an aggressive chemical environment.

5) Minimum mean pore radius was observed in the dense microstructure at a low W/B ratio (0.3), giving lower porosity and tortuosity in the high-performance mixture. Whereas mixes with W/B ratio > 0.4 gave the maximum tortuosity value indicating a more interconnected pore network and thereby poor performance in strength and durability compared to lower W/B ratios.

6) Maximum strength and durability values were observed in mixes at 0.3 W/B ratios in R15NS1.5. However, in the same mix at a 0.4 W/B ratio, the strength and durability values are near the conventional mixes.

#### ACKNOWLEDGEMENTS

This work was financially supported with a seed grant by the Vellore Institute of Technology, Vellore (Seed no.SG20210204). The authors gratefully acknowledge the testing labs of Vellore Institute of Technology, Vellore, for supplying facilities to carry out this research work. We are also grateful to Dr. Sushant Kishore, Assistant professor, School of Social Science and Languages, Vellore Institute of Technology, Vellore, for proof reading and improved the manuscript significantly.

#### AUTHOR CONTRIBUTIONS:

Conceptualization: T. Shanmugapriya. Data curation: K. Athira. Formal analysis: T. Shanmugapriya. Funding acquisition: T. Shanmugapriya. Investigation: T. Shanmugapriya. Methodology: K. Athira. Project administration: K. Athira. Resources: K. Athira. Supervision: T. Shanmugapriya. Validation: K. Athira. Visualization: K. Athira, T. Shanmugapriya. Writing, original draft: K. Athira. Writing, review & editing: T. Shanmugapriya.

## REFERENCES

- Aayog, N. (2019) Resource efficiency and circular economy -Current status and way forward.
- Patel, S.; Pal, B.K. (2015) Current status of an industrial waste: Red mud an overview. *Int. J. Latest Technol. Eng. Manag. Appl. Sci.* 4, 1–16. Retrieved from: <https://paratechglobal.com/wp-content/uploads/2020/01/Current-Status-of-an-Industrial-Waste-Re.pdf>.
- Hyeok-Jung, K.; Kang, S-P.; Choe, G-C. (2018) Effect of red mud content on strength and efflorescence in pavement using alkali-activated slag cement. *Int. J. Concr. Struct. Mater.* 12, 18. <https://doi.org/10.1186/s40069-018-0258-3>.
- Krivenko, P.; Kovalchuk, O., Pasko, A.; Croymans, T.; Hult, M.; Lutter, G.; Vandevenne, N.; Schreurs, S.; Schroyers, W. (2017) Development of alkali activated cements and concrete mixture design with high volumes of red mud. *Constr. Build. Mater.* 151, 819–826. <https://doi.org/10.1016/j.conbuildmat.2017.06.031>.
- Nikbin, I.M.; Aliaghazadeh, M.; Charkhtab, Sh.; Fathollahpour, A. (2016) Environmental impacts and mechanical properties of lightweight concrete containing bauxite residue (red mud) *J. Clean. Prod.* 127, 2683–2694. <https://doi.org/10.1016/j.jclepro.2017.11.143>.
- de Oliveira Romano, R.C.; Bernardo, H.M.; Maciel, M.H.; Pileggi, R.G.; Cincotto, M.A. (2019) Using isothermal calorimetry, X-ray diffraction, thermogravimetry and FTIR to monitor the hydration reaction of Portland cements associated with red mud as a supplementary material. *J. Therm. Anal. Calorim.* 137, 1877–1890. <https://doi.org/10.1007/s10973-019-08095-x>.
- Tang, W.C.; Wang, Z.; Liu, Y.; Cui, H.Z. (2018) Influence of red mud on fresh and hardened properties of self-compacting concrete. *Constr. Build. Mater.* 178, 288–300. <https://doi.org/10.1016/j.conbuildmat.2018.05.171>.
- Yadav, V.S.; Prasad, M.; Khan, J.; Amritphale, S.S.; Singh, M.; Raju, C.B. (2010) Sequestration of carbon dioxide (CO<sub>2</sub>) using red mud. *J. Hazard. Mater.* 176, 1044–1050. <https://doi.org/10.1016/j.jhazmat.2009.11.146>.
- Liu, R.X.; Poon, C-S. (2016) Utilization of red mud derived from bauxite in self-compacting concrete. *J. Clean. Prod.* 112, 384–391. <https://doi.org/10.1016/j.jclepro.2015.09.049>.
- Canbek, O.; Shakouri, S.; Erdoğan, S.T. (2020) Laboratory production of calcium sulfoaluminate cements with high industrial waste content. *Cem. Concr. Compos.* 106, 103475. <https://doi.org/10.1016/j.cemconcomp.2019.103475>.
- Dodoo-Arhin, D.; Nuamah, R.A.; Agyei-Tuffour, B.; Obada, D.O.; Yaya, A. (2017) Awaso bauxite red mud-cement based composites: Characterisation for pavement applications. *Case Stud. Constr. Mater.* 7, 45–55. <https://doi.org/10.1016/j.cscm.2017.05.003>.
- Wu, C-s.; Liu, D-y. (2012) Mineral phase and physical properties of red mud calcined at different temperatures. *J. Nanomater.* 2012, 628592. <https://doi.org/10.1155/2012/628592>.
- Ghalehnovi, M.; Roshan, N.; Hakak, E.; Shamsabadi, E.A.; de Brito, J. (2019) Effect of red mud (bauxite residue) as cement replacement on the properties of self-compacting concrete incorporating various fillers. *J. Clean. Prod.* 240, 118213. <https://doi.org/10.1016/j.jclepro.2019.118213>.
- Ghalehnovi, M.; Asadi Shamsabadi, E.; Khodabakhshian, A.; Sourmeh, F.; de Brito, J. (2019) Self-compacting architectural concrete production using red mud. *Constr. Build. Mater.* 226, 418–427. <https://doi.org/10.1016/j.conbuildmat.2019.07.248>.
- Hou, D.; Wu, D.; Wang, X.; Gao, S.; Yu, R.; Li, M.; Wang, P.; Wang, Y. (2021) Sustainable use of red mud in ultra-high performance concrete (UHPC): Design and performance evaluation. *Cem. Concr. Compos.* 115, 103862. <https://doi.org/10.1016/j.cemconcomp.2020.103862>.
- Agrawal, V.; Paulose, R.; Arya, R.; Rajak, G.; Giri, A.; Bijanu, A.; Sanghi, S.K.; Mishra, D.; N, P.; Khare, A.K.; Parmar, V.; Khan, M.A.; Bhisikar, A.; Srivastava, A.K.; Thankaraj Salammal, S. (2022) Green conversion of hazardous red mud into diagnostic X-ray shielding tiles. *J. Hazard. Mater.* 424, 127507. <https://doi.org/10.1016/j.jhazmat.2021.127507>.
- Matyka, M.; Koza, Z. (2011) How to calculate tortuosity easily? *AIP Conf. Proc.* 1453, 17–22. <https://doi.org/10.1063/1.4711147>.
- Kondraivendhan, B.; Sabet Divsholi, B.; Teng, S. (2013) Estimation of strength, permeability and hydraulic diffusivity of pozzolana blended concrete through pore size distribution. *J. Adv. Concr. Technol.* 11, 230–237. <https://doi.org/10.3151/jact.11.230>.
- Muthu, M.; Santhanam, M. (2018) Effect of reduced graphene oxide, alumina and silica nanoparticles on the deterioration characteristics of Portland cement paste exposed to acidic environment. *Cem. Concr. Compos.* 91, 118–137. <https://doi.org/10.1016/j.cemconcomp.2018.05.005>.
- Chithra, S.; Senthil Kumar, S.R.R.; Chinnaraju, K. (2016) The effect of Colloidal Nano-silica on workability, mechanical and durability properties of High Performance Concrete with Copper slag as partial fine aggregate. *Constr. Build. Mater.* 113, 794–804. <https://doi.org/10.1016/j.conbuildmat.2016.03.119>.
- Kong, D.; Corr, D.J.; Hou, P.; Yang, Y.; Shah, S.P. (2015) Influence of colloidal silica sol on fresh properties of cement paste as compared to nano-silica powder with agglomerates in micron-scale. *Cem. Concr. Compos.* 63, 30–41. <https://doi.org/10.1016/j.cemconcomp.2015.08.002>.
- Kong, D.; Pan, H.; Wang, L.; Corr, D.J.; Yang, Y.; Shah, S.P.; Sheng, J. (2019) Effect and mechanism of colloidal silica sol on properties and microstructure of the hardened cement-based materials as compared to nano-silica powder with agglomerates in micron-scale. *Cem. Concr. Compos.* 98, 137–149. <https://doi.org/10.1016/j.cemconcomp.2019.02.015>.
- Gaitero, J.J.; Campillo, I.; Guerrero, A. (2008) Reduction of the calcium leaching rate of cement paste by addition of silica nanoparticles. *Cem. Concr. Res.* 38, 1112–1118. <https://doi.org/10.1016/j.cemconres.2008.03.021>.
- Li, L.G.; Zheng, J.Y.; Ng, P.L.; Zhu, J.; Kwan, A.K.H. (2019) Cementing efficiencies and synergistic roles of silica fume and nano-silica in sulphate and chloride resistance of concrete. *Constr. Build. Mater.* 223, 965–975. <https://doi.org/10.1016/j.conbuildmat.2019.07.241>.
- IS 516. (2018) Method of tests for strength of concrete. *Bur. Indian Stand. Dehli.* 1–30.
- ASTM C642. (1997) Standard test method for density, absorption, and voids in hardened concrete, ASTM International, United States. Annu. B. ASTM Stand. 1–3.
- Casnedi, L.; Cocco, O.; Meloni, P.; Pia, G. (2018) Water absorption properties of cement pastes: Experimental and modelling inspections. *Adv. Mater. Sci. Eng.* 2018, 7679131. <https://doi.org/10.1155/2018/7679131>.
- Du, H.; Pang, S.D. (2019) High performance cement composites with colloidal nano-silica. *Constr. Build. Mater.* 224, 317–325. <https://doi.org/10.1016/j.conbuildmat.2019.07.045>.
- Venkatanarayanan, H.K.; Rangaraju, P.R. (2014) Evaluation of sulfate resistance of Portland cement mortars containing low-carbon rice husk ash. *J. Mater. Civ. Eng.* 26, 582–592. [https://doi.org/10.1061/\(asce\)jmt.1943-5533.0000868](https://doi.org/10.1061/(asce)jmt.1943-5533.0000868).
- Chen, F.; Gao, J.; Qi, B.; Shen, D. (2017) Deterioration mechanism of plain and blended cement mortars partially exposed to sulfate attack. *Constr. Build. Mater.* 154, 849–856. <https://doi.org/10.1016/j.conbuildmat.2017.08.017>.
- Lee, S.T.; Moon, H.Y.; Swamy, R.N. (2005) Sulfate attack and role of silica fume in resisting strength loss. *Cem. Concr. Compos.* 27, 65–76. <https://doi.org/10.1016/j.cemconcomp.2003.11.003>.
- Chatveera, B.; Lertwattanaruk, P. (2009) Evaluation of sulfate resistance of cement mortars containing black rice husk ash. *J. Environ. Manage.* 90, 1435–1441. <https://doi.org/10.1016/j.jenvman.2008.09.001>.
- Andrade, C.; D'Andrea, R.; Rebolledo, N. (2012) Calculation of tortuosity factor for the model based in concrete resistivity. *Second Int. Conf. Microstruct. Durab. Cem. Compos.* 11–13.
- Powers, T.C. (1958) Structure and physical properties of hardened Portland cement paste. *J. Am. Ceram. Soc.* 41,

- 1-6. <https://doi.org/10.1111/j.1151-2916.1958.tb13494.x>.
35. Yang, L.; Gao, D.; Zhang, Y.; Tang, J.; Li, Y. (2019) Relationship between sorptivity and capillary coefficient for water absorption of cement-based materials: *theory analysis and experiment*. *R. Soc. Open Sci.* 6, 190112. <https://doi.org/10.1098/rsos.190112>.
36. Kondraivendhan, B.; Bhattacharjee, B. (2010) Effect of age and water-cement ratio on size and dispersion of pores in ordinary portland cement paste. *ACI Mater. J.* 107, 147–154. <https://doi.org/10.14359/51663578>.